eprints@whiterose.ac.uk
https://eprints.whiterose.ac.uk/

1 **Mercury anomalies across the end Permian mass extinction in South China from**

2 **shallow and deep water depositional environments**

3

4 **Xiangdong Wang[1], Peter A. Cawood[2,3], He Zhao[1], Laishi Zhao[1,] *, Stephen E.**

5 **Grasby[4], Zhong-Qiang Chen[5,] *, Paul B. Wignall[6], Zhengyi Lv[1], Chen Han[1]**

6 [1] State Key Laboratory of Geological Processes and Mineral Resources, China

7 University of Geosciences (Wuhan), Wuhan 430074, China.

8 [2] Department of Earth, Atmosphere and Environment, Monash University, Victoria

9 3800, Australia

10 [3] Department of Earth Sciences, University of St Andrew, KY16 9AL, UK

11 [4] Geological Survey of Canada, Natural Resources Canada, Calgary, Alberta T2L2A7,

12 Canada

13 [5] State Key Laboratory of Biogeology and Environmental Geology, China University

14 of Geosciences (Wuhan), Wuhan 430074, China

15 [6] School of Earth and Environment, University of Leeds, Leeds, UK

16 * Correspondent authors, E-mails: lszhao@cug.edu.cn, zhong.qiang.chen@cug.edu.cn

17 **Abstract**

18 Life on Earth suffered its greatest bio-crisis since multicellular organisms rose 600

19 million years ago during the end-Permian mass extinction. Coincidence of the mass

20 extinction with flood basalt eruptions in Siberia is well established, but the exact

21 causal connection between the eruptions and extinction processes in South China is

uncertain due to their wide spatial separation and the absence of direct geochemical

evidence linking the two. The concentration and stable isotope analysis of mercury

provides a way to test these links as its concentration is thought to be tied to igneous

activity. Mercury/total organic carbon ratios from three Permian-Triassic boundary

sections with a well-resolved extinction record in South China show elevated values

(up to 900 ppb/wt. % relative to a background of <100 ppb/wt. %) that exactly

coincides with the end-Permian mass extinction horizon. This enrichment does not

show any correlation with redox and sedimentation rate variations during that time.

Hg isotope mass-independent fractionation (Δ^{199}Hg), with sustained positive values,

indicate a predominant atmospheric-derived signature of volcanic Hg in deep-shelf

settings of the Daxiakou and Shangsi sections. In contrast, the nearshore environment

of the Meishan section displays a negative Δ^{199}Hg signature, interpreted to be related

to terrestrial Hg sources. Such temporal differences in Δ^{199}Hg values shed new light

on Hg geochemical behavior in marine settings, and also on kill mechanisms

associated with volcanism that were responsible for biotic mortality at the end of the

Permian.

1. Introduction

The end-Permian mass extinction (EPME; 252 million years ago) was the most

severe biotic crisis of the Phanerozoic. Most workers agree that intense volcanic

activity of the Siberian Traps Large Igneous Province (STLIP) was a driver of

43 environmental change (Wignall, 2001; Svensen et al., 2009; Sun et al., 2012; Black et

44 al., 2014; Clarkson et al., 2015; Burgess et al., 2017). The STLIP has an estimated

45 volume of up to $3–4 \times 10^6$ km^3, which is larger than any other continental basalt

46 province, including the Emeishan traps ($\sim 1 \times 10^6$ km^3), Central Atlantic Magmatic

47 Province ($\sim 2 \times 10^6$ km^3), Karoo and Ferrar traps ($\sim 2.5 \times 10^6$ km^3) and Deccan traps

48 ($2–4 \times 10^6$ km^3) (Courtillot and Renne, 2003, references therein). Its original volume

49 is likely considerably larger as most is buried and inaccessible beneath the younger

50 sediments of the West Siberian Basin (Reichow et al., 2009; Saunders, 2016). Recent

51 high-precision U-Pb dating of STLIP basalts have shown that the onset of eruptions

52 began shortly before the start of the mass extinction crisis (Burgess and Bowring,

53 2015). More recently, Burgess et al. (2017) further categorized the dated volcanic

54 rocks from STLIP into lava- and sill-originated rocks, and found that major transfer

55 from lava to sill eruptions coincided with the main episode of biotic extinction.

56 Although there is a clear temporal correlation between the extinction event and

57 volcanic activity, the precise mechanism that drove the environmental change is

58 unresolved. In recent years, stable isotope systems have been shown to provide

59 important insights into the response of environmental systems to key climatic changes

60 associated with extinction events (Payne et al., 2010; Clarkson et al., 2015; Song et al.,

61 2017; Liu et al., 2017). For example, calcium and boron isotopes were successfully

62 applied to demonstrate ocean acidification triggered by STLIP across the EPME

63 (Payne et al., 2010; Clarkson et al., 2015). But for any isotopic system there are often

64 multiple inputs and outputs that can control the isotopic fractionation process in the

65 environment. In this paper we attempt to evaluate environmental controls on Hg

66 associated with the EPME. Hg is a key gas associated with volcanic activity and has

67 been linked to the end-Permian environmental crisis (Sanei et al., 2012; Grasby et al;

68 2013, 2017)–a link we aim to assess here using mercury concentrations and isotopes

69 measured in Permian-Triassic boundary (PTB) sections in South China.

70   The ratio of mercury concentrations over total organic carbon (Hg/TOC) in

71 sedimentary sections has been shown to provide a proxy for voluminous volcanism

72 (Sanei et al., 2012; Grasby et al., 2013, 2017). Mercury is a highly toxic heavy metal

73 and has a sufficiently long atmospheric residence time (>1.5 yr) for global distribution

74 (Blum et al., 2014). Explosive volcanic events inject abundant Hg into the atmosphere

75 ensuring its global reach (Pyle and Mather, 2003). Most volcanic mercury is released

76 as gaseous Hg^0 and removed from the atmosphere mainly through oxidation to form

77 Hg^{2+}, which then accumulates in oceans and on land through rainfall or adsorption

78 onto organic matter ensuring a strong association between Hg and TOC in sediments

79 (Gehrke et al., 2009; Ruiz and Tomiyasu, 2015). Hg isotopes can undergo both large

80 mass-dependent fractionations (MDF) and mass-independent fractionations (MIF) in

81 nature (Blum et al., 2014), and thus are capable of tracing Hg sources and cycling

82 (Grasby et al., 2017). Hg-MDF (δ^{202}Hg) can result from many pathways, including

83 physical, chemical and biological reactions, whereas Hg-MIF (Δ^{199}Hg) is controlled

84 by more limited pathways (mostly photochemical) and is unlikely to be altered in the

85 post-depositional processes (Blum et al., 2014; Thibodeau et al., 2016; Thibodeau and

86 Bergquist, 2017). Hence, Hg-MIF (Δ^{199}Hg) is generally a more conservative tracer of

87   volcanic signature (Thibodeau and Bergquist, 2017).

88   In recent years, Hg concentrations and isotopes have been used to explore the

89   relationship between large igneous provinces and contemporary mass extinctions

90   (Sanei et al., 2012; Grasby et al; 2013, 2017; Percival et al., 2015, 2017; Sial et al.,

91   2016; Thibodeau et al., 2016; Gong et al., 2017). Anomalous Hg deposition was

92   observed at the EPME crisis in the Sverdrup Basin, Canadian High Arctic that

93   occupied a paleogeographic position near the STLIP (Fig. 1A) (Sanei et al., 2012;

94   Grasby et al., 2013). More recently, Grasby et al. (2017) documented the difference in

95   Hg isotopes near the EPME between Sverdrup Basin at a deep water setting and the

96   shallower water Meishan section in South China. They attributed the negative Δ^{199}Hg

97   values at the EPME in Meishan to terrestrial sources, and suggested that deeper water

98   sections that are isolated from terrestrial input provide better records of the volcanic

99   signature. Therefore, whether or not the signature of Hg enrichments associated with

100   STLIP is recorded in the South China sections is unresolved. We further this work by

101   examining a series of sections in South China covering a range of water depths. We

102   provide new data for two deeper-water sections (200–500m), at Daxiakou and

103   Shangsi in South China, and integrate this with the data from the shallow water

104   Meishan section (Grasby et al., 2017). We measured Hg concentrations and Hg

105   isotopic compositions through the Clarkina changxingensis (C. changxingensis) to

106   Isarcicella isarcica (I. isarcica) conodont zones, to clarify the timing and intensity of

107   the eruption across the PTB and link its relationship with EPME in South China. The

108   varied sedimentary environments in the three sections enable an assessment of the

109   geochemical behaviors of Hg in different water depths and indicated that the effects of

110   the STLIP extended to the Chinese sections.

111

2. Geological background

113   The Meishan, Daxiakou, and Shangsi sections are separated by over 1000 km and lie

114   along the northern part of South China Craton. During late Permian time, the craton

115   was situated at low latitudes in the eastern Paleo-Tethys (Fig. 1A).The craton was

116   characterized by marine facies in its interior, and bounded by lands to the east and

117   west (Fig. 1B). In the central part of the craton, the roughly east-west trending

118   Yangtze carbonate platform is flanked to the north and south by deeper water basins

119   (Feng et al., 1996; Fig. 1B). The three studied sections lie on the flanks of the

120   northern basin and the EPME has been calibrated at the bottom of the C. meishanensis

121   conodont zone, with the PTB was placed at the bottom of the Hindeodus parvus (H.

122   parvus) conodont zone (Jiang et al., 2011; Zhao et al., 2013; Chen et al., 2015).

123   The Meishan section, which is located at Meishan Town, Changxing County,

124   Zhejiang Province, lay on the northeastern margin of the Yangtze Platform at a

125   shallow water depth of between 30–60 m based on sedimentary structures indicative

126   of fair-weather wave base and storm wave base (Yin et al., 2001; Chen et al., 2015;

127   Fig. 1B). This section is the Global Stratotype of Point and Section (GSSP) for the

128   PTB (Yin et al., 2001). Biostratigraphy, lithofacies, geochronology, and geochemistry

129   of the Meishan section have been extensively investigated since the 1980's, and have

130   been updated by Chen et al. (2015). Herein, the uppermost Permian succession (Beds

131   20–24) consists of bioclastic limestone of the Changxing Formation, whereas the

132   lowest Triassic strata consist of calcareous mudstone and marlstone of the Yinkeng

133   Formation (Beds 25–51) (Chen et al., 2015).

134   The Daxiakou section is situated near the town of Xiakou, Xingshan County,

135   Hubei province. This section was deposited on the northern margin of the South

136   China craton in a relatively deeper-water (~200–500 m) basin setting, as determined

137   by conodont biofacies and deeper-water foraminifera (Zhao et al., 2013; Zhang and

138   Gu, 2015; Fig. 1B). The uppermost Permian succession is dominated by black shale

139   with scattered interbeds of limestone and volcanic tuff of the Dalong Formation,

140   whereas the lowest Triassic sequence is composed of thin-bedded limestone and

141   calcareous mudstone interbeds of volcanic tuff of the Daye Formation. Zhao et al.

142   (2013) established the detailed conodont zonation at Daxiakou, which correlates well

143   with the Meishan section. Li et al. (2016) have also established high-resolution

144   astronomical cycles for the PTB beds in the same section.

145   The Shangsi section, one of the candidate sections for the GSSP of the PTB, is

146   located near Changjianggou village of Shangsi Town, Guangyuan City, Sichuan

147   Province. The Shangsi area lay on the northwestern margin of the South China craton

148   (Fig. 1B). The PTB succession is continuously exposed at this section and has been

149   well studied (Li et al., 1986; Wignall et al., 1995; Riccardi et al., 2007; Jiang et al.,

150   2011; Shen et al., 2011; Xiang et al., 2016). The latest Permian succession is mainly

151   composed of siliceous limestone interbedded with black shale of the Dalong

7

152   Formation, indicating that it represents a relatively deeper-water setting which is

153   supported by deep-water radiolarian assemblages (~200–500 m) (Jiang et al., 2011;

154   Xiao et al., 2017; Fig. 1B). However, the water-depth gradually started to shallow

155   from the latest Permian (Li et al., 1986). At the EPME, the lithology changed from

156   siliceous limestone to mudstone. The lowest Triassic strata mainly consist of interbeds

157   of marlstone and mudstone of the Feixianguan Formation.

158

159   **3. Methods**

160   3.1 Mercury concentrations

161   Mercury content was measured using a LECO AMA254 mercury analyzer at the

162   State Key Laboratory of Geological Processes and Mineral Resources (SKLGPMR),

163   China University of Geosciences (CUG-Wuhan). Prior to analysis, all samples were

164   freeze-dried to prevent decomposition of Hg. About 100 mg of mudstone or shale and

165   150–200 mg of limestone were analyzed. Data reliability was ensured by use of

166   international standard 502-685 (0.04 ± 0.008 ppm), which was analyzed after every

167   12 unknowns then followed by a repeat. The analytic precision is within 5 % and

168   reproducibility of sample concentrations was within 10 %.

169

170   3.2 Total organic carbon (TOC) measurement

171   TOC content measurement was conducted in the SKLGPMR (CUG, Wuhan) by

172   a vario macro cube elemental analyzer. About 10 g of powdered sample was put into

173　the 50 mL tube, then 50 % HCl was injected to dissolve carbonate minerals until there

174　was no further bubbling. After multiple centrifugal and lyophilization, the residue was

175　analyzed for total organic carbon (TOC). Data quality was assessed through multiple

176　analyses of standard sample DP-1 (65.44±0.33 %). A standard sample and a repeat

177　were analyzed after every 12 unknowns, yielding an analytical accuracy of 2.5 % of

178　the reported values.

179

180　3.3 Hg isotopes

181　　Hg isotopic compositions of samples from the three sections were analyzed at the

182　Institute of Geochemistry, Chinese Academy of Sciences, Guiyang, China. Detailed

183　analytical methods and processing procedure follow those described by Grasby et al.

184　(2017) and Gong et al. (2017). Approximately 0.5 g of ground sample and ~0.1 g of

185　standard reference materials (GSS-4, soil) were digested (95 °C for 90 min) using 5

186　mL of aqua regia ($HCl/HNO3 = 3$, v/v). After digestion, the solution was centrifuged

187　(3000 rpm for 10 min) at room temperature and then decanted to obtain the

188　supernatant. Before conducting Hg isotope analysis, the digested sample solutions

189　were diluted to 2 and 1 ng mL^{-1} using Milli-Q water based on total Hg values. All the

190　acid concentrations of the diluted solutions were < 20 %. Similarly, NIST SRM 3133

191　and 3177 Hg standard solutions with Hg concentrations of 2 and 1ng mL^{-1} were also

192　prepared.

193　　Isotopic values were measured using a Neptune MC-ICP-MS with high

194　sensitivity X skimmer cone. NIST SRM 997 Tl was the internal standard used for

195   simultaneous instrumental mass bias correction of Hg. $SnCl_2$ (4 ng mL^{-1}) was used to

196   generate elemental $Hg^{(0)}$ before being introduced into the plasma. The stability of the

197   instrument and measurement precision were monitored using NIST SRM 3133 and

198   3177 Hg standard solutions, respectively. Sample-standard bracketing was based on

199   NIST 3133. Digest recovery of the samples was monitored by MC-ICP-MS using

200   ^{202}Hg signals. The sensitivity for ^{202}Hg during Hg isotope analysis was ~1.2 V per ng

201   mL^{-1} Hg.

202   Hg isotopic variations are reported in $\delta^{202}Hg$ notation in units of per mil (‰)

203   referenced to the NIST-3133 Hg standard (once every 3 samples):

204

205    $\delta^{202}Hg (‰)= [(^{202}Hg/^{198}Hg_{sample})/(^{202}Hg/^{198}Hg_{standard}) -1]\times1000$ (1)

206

207   Mass independent fractionation (MIF) of Hg isotopes is expressed in Δ notation

208   ($\Delta^{xxx}Hg$), which describes the difference between the measured $\delta^{xxx}Hg$ and the

209   theoretically predicted $\delta^{xxx}Hg$ value, using the following equations:

210

211    $\Delta^{199}Hg \approx \delta^{199}Hg - (\delta^{202}Hg \times 0.2520)$ (2)

212    $\Delta^{200}Hg \approx \delta^{200}Hg - (\delta^{202}Hg \times 0.5024)$ (3)

213    $\Delta^{201}Hg \approx \delta^{201}Hg - (\delta^{202}Hg \times 0.7520)$ (4)

214

215   Replicate analysis of the NIST 3177 Hg intra lab isotope reference standard (n = 4

216   analytical sessions) were as follows: $\delta^{202}Hg$ = -0.42 ± 0.06‰ (2 sd); $\Delta^{199}Hg$ = -0.04 ±

217   0.02‰ (2 sd); $\Delta^{200}Hg = 0.01 \pm 0.04$‰ (2 sd); $\Delta^{201}Hg = 0.01 \pm 0.04$‰ (2 sd).

218   The complete data set of Hg, TOC, Hg/TOC and Hg isotopes values can be

219   obtained in Online Supplementary Tables S1, S2, S3.

220

221   **4. Results**

222   4.1 TOC contents

223   In the Meishan section, TOC concentrations vary from 0.06 to 1.56 wt. %, and

224   have relatively higher values (~1 wt. %) at the bottom of Bed 22 and Beds 24–26,

225   44–49 (Fig. 2). Through the Daxiakou section, TOC concentrations range from 0.04 to

226   3.99 wt. %. The latest Permian rocks of Dalong Formation show very high TOC

227   concentrations (~4.0 wt. %; Fig. 3). While the earliest Triassic Daye Formation

228   display low TOC concentrations, almost all less than 1 wt. %. In the Shangsi section,

229   the TOC concentrations vary from 0.03 to 2.82 wt. %. The higher TOC values (~1

230   wt. %) occurs the bottom of Bed 22 of the Dalong Formation and Beds 30–33 in Daye

231   Formation (Fig. 4). In other horizons, TOC has lower values (mostly less than 0.4

232   wt. %).

233

234   4.2 Hg and Hg/TOC variations

235   The Meishan, Daxiakou and Shangsi sections all record high Hg concentrations

236   and a short-lived positive excursion in Hg/TOC values coincident with the EPME. Hg

237   concentrations are directly tied to TOC contents (Grasby et al., 2013), and this is

238   demonstrated by the covariant relationship between TOC and Hg concentrations of

239   the studied sections where Daxiakou and Shangsi have the highest Hg values in the

240   late Permian along with anomalously high TOC contents (Figs. 2, 3, 4).

241   In the Meishan section, the highest Hg values (up to 176 ppb) occur at the top of

242   Bed 24 and in Beds 25–26. High values also occur at the bottom of Bed 22 and Beds

243   44–49. TOC values are high in these layers, indicating the Hg concentrations are

244   probable driven by lithologically controlled changes in organic matter content.

245   Compared to Hg concentrations, positive excursions in Hg/TOC are only observed in

246   the uppermost parts of Bed 24 and Bed 25, corresponding to the EPME (Fig. 2). In the

247   Daxiakou section, the uppermost Dalong Formation (Bed 9), in the C. meishanensis

248   conodont zone, corresponds to Bed 25 in the Meishan section and records high values

249   in Hg concentrations (~300 ppb) and a positive excursion in Hg/TOC ratios (Fig. 3).

250   High Hg concentrations are also present through the upper Permian of the Dalong

251   Formation, although in these layers there is no Hg/TOC excursion (Fig. 3). This may

252   imply that the high Hg contents are due to high levels of TOC in the shale. Similar to

253   TOC, high Hg concentrations also occur at the bottom of Bed 22 and Beds 30-33 in

254   the Shangsi section (Fig. 4), except near the EPME where high Hg values (~100 ppb)

255   were recorded, whereas TOC contents are relatively low. A Hg/TOC excursion was

256   only recorded near the EPME.

257

258   4.3 Hg isotope compositions of the study sections

259   The Hg isotope values of the Meishan, Daxiakou and Shangsi sections are

260   shown in figures 2, 3, and 4, respectively, and analytical results are also provided in

261   Online Supplementary Tables S1, S2, and S3.

262   MDF (δ^{202}Hg) at Meishan ranges from -2.3 ‰ to -0.58 ‰, and MIF (Δ^{199}Hg)

263   varies from -0.12 ‰ to 2.0 ‰. They both show negative shifts at the EPME (to -1.74 ‰

264   in δ^{202}Hg and -0.12 ‰ in Δ^{199}Hg; Fig. 2). MDF (δ^{202}Hg) also shows similar negative

265   values above and below the EPME. MDF (δ^{202}Hg) values at Daxiakou are negative

266   and vary from -1.78 ‰ to -0.49 ‰. The values rise below the EPME (to -0.49 ‰) and

267   decline above it (Fig. 3). MIF (Δ^{199}Hg) values vary through the section, from -0.02 ‰

268   to 0.27 ‰. For uppermost Permian samples, Δ^{199}Hg values are relatively high and

269   have an average of 0.18 ‰. The high values continue through the EPME and drop

270   below 1.0 ‰ in the earliest Triassic. Overall, Δ^{199}Hg values at Daxiakou display

271   positive values with no significant change across the EPME (Fig. 3). At the Shangsi

272   section, MDF (δ^{202}Hg) and MIF (Δ^{199}Hg) values range from -2.26 ‰ to -0.58 ‰, and

273   -0.01 ‰ to 0.21 ‰, respectively. The Δ^{199}Hg values are similar to those at Daxiakou,

274   with high values in uppermost Permian samples and lower values in the earliest

275   Triassic, and also show sustained positive values across the EPME (Fig. 4). The main

276   difference between these two sections is that greater MDF (δ^{202}Hg) and MIF (Δ^{199}Hg)

277   levels are reached at the EPME in Daxiakou. The maximum δ^{202}Hg and Δ^{199}Hg at the

278   EPME in the Shangsi section are -0.75 ‰ and 0.11 ‰, respectively, whereas the

279   maximum values at Daxiakou are -0.49 ‰ and 0.15 ‰.

280

5. Discussion

5.1 Cause of the Hg and Hg/TOC anomalies

High Hg concentrations and elevated Hg/TOC values are all recorded across the EPME in the studies of the Meishan, Daxiakou and Shangsi sections. Background Hg concentrations are directly tied to marine organic matter (OM) deposition rates. For example, high Hg values are observed at the bottom of Bed 22, and Beds 44–49 in Meishan, through the upper Permian Dalong Formation at Daxiakou, and at the bottom of Bed 22 and Beds 30–33 at Shangsi, and all are associated with high TOC contents in shale or siliceous limestone. A constant and low Hg/TOC ratio is a common feature of background marine conditions (Grasby et al., 2013, 2017). Our results also show a pronounced increase in Hg/TOC values coincident with the extinction interval (Figs. 2–5).

The role of lithology, sedimentation rate, and marine anoxia on Hg/TOC values must all be considered to explain these shifts, because all are known to vary in the studied sections. Lithologic variations are pronounced near the EPME and include bioclastic limestone, mudstone, shale and volcanic ash beds, but there is no relationship to the Hg/TOC changes. Within the C. meishanensis conodont zone at Daxiakou for example, constant high Hg/TOC values were recorded in different lithologic samples, including volcanic ash, shale, mudstone and limestone. In addition to lithology, if the atmospheric mercury level is constant, a reduced sedimentation rate may result in elevated Hg concentrations (Percival et al, 2015). This affect can be accounted for by comparison with TOC concentrations, as these would also covary

303 with sedimentation rates (e.g. dilution effects). Using a recently-devised

304 cyclostratigraphic scheme (Li et al., 2016), sedimentation rates in the Meishan and

305 Daxiakou sections do indeed vary substantially (Fig. 2, 3). This reveals though that

306 there is no clear correlation between Hg/TOC values and sedimentation rate. Marine

307 anoxia was also widespread during the PTB transition, and its intensity varied

308 considerably. The PTB transition saw the temporary establishment of oxic/weakly

309 dysoxic conditions in Meishan (Chen et al., 2015) whereas the deeper-water Shangsi

310 and Daxiakou sections saw more oxygen-restricted conditions (Xiang et al., 2016;

311 Shen et al., 2016). The Hg/TOC fluctuations are not influenced by these oxygenation

312 trends, the highest values only occur at the EPME (Beds 27) in Shangsi (Fig. 4),

313 indicating that redox conditions have no significant control.

314   The Hg isotopic compositions can help to trace the origin and the pathways of

315 the observed Hg and Hg/TOC excursions (Thibodeau et al., 2016; Grasby et al., 2017;

316 Gong et al.,2017). Volcanic Hg has δ^{202}Hg values between -2.0 ‰ and 0 ‰, and has

317 insignificant MIF (Δ^{199}Hg ≈ 0 ‰) (Zambardi et al., 2009; Yin et al., 2016; Grasby et

318 al., 2017; Thibodeau and Bergquist, 2017). Once emitted to the environment, MDF

319 (δ^{202}Hg) can result in indistinguishable signatures from many pathways, including

320 hydrothermal reactions, sorption/deposition, organic matter burial and diagenesis

321 (Blum et al., 2014; Thibodeau et al., 2016; Grasby et al., 2017). In contrast, MIF

322 (Δ^{199}Hg) mostly occurs through photochemical reduction, such as in aqueous droplets

323 and surface waters, resulting in positive Δ^{199}Hg values (Bergquist and Blum, 2007;

324 Blum et al., 2014). Aquatic environments can receive Hg through atmospheric Hg^{2+}

325   deposition and direct uptake of $Hg^0_{(g)}$ by terrestrial sources (Thibodeau and Bergquist,

326   2017). Thus, marine sediments dominated by atmospheric Hg^{2+} deposition tend to

327   have positive $\Delta^{199}Hg$ because of the photo reduction in the surface environments

328   (Grasby et al., 2017; Thibodeau and Bergquist, 2017). However, sediments that

329   received $Hg^0_{(g)}$ through terrestrial runoff tend to have greater negative $\delta^{202}Hg$ and

330    $\Delta^{199}Hg$ than atmospheric $Hg^0_{(g)}$, and terrestrial resources acquire negative $\delta^{202}Hg$ and

331    $\Delta^{199}Hg$ values when plants and soils sequestrate $Hg^0_{(g)}$ (Thibodeau and Bergquist,

332   2017). In our study, the two relatively deeper water sections, Daxiakou and Shangsi,

333   both recorded higher Hg/TOC values and sustained positive $\Delta^{199}Hg$ values at the

334   EPME (Fig. 3, 4). This finding is consistent with the data of coeval Buchanan lake

335   sediments (deep water facies) that show positive $\Delta^{199}Hg$ values with no significant

336   change across the EPME despite a large Hg spike (Grasby et al., 2017). The

337   excursions in Hg/TOC indicate that increased Hg flux was imported to the oceans at

338   that time. Meanwhile, the positive $\Delta^{199}Hg$ values indicate sediments in these deep

339   water sections received Hg primarily through atmospheric Hg deposition, instead of

340   terrestrial runoff. Thus, the observed Hg peaks are due to enhanced flux of Hg from

341   atmosphere consistent with enhanced atmospheric content. The best way to explain

342   this is that enhanced volcanic activity injected massive quantities of Hg into the

343   atmosphere and increased the global atmospheric Hg level.

344

345   5.2 Variations of Hg/TOC values and Hg isotopic compositions in different water

346   depths

347   The Meishan, Daxiakou and Shangsi sections all showed short-duration, albeit

348   variable, positive excursions, in Hg/TOC across the EPME (Figs. 2–5). The maximum

349   Hg/TOC at Meishan, Shangsi and Daxiakou are 926 ppb/wt. %, 553 ppb/wt. %, and

350   254 ppb/wt. %, respectively. The prominent negative shifts of δ^{202}Hg and Δ^{199}Hg

351   values at the EPME horizon in the Meishan section (Fig. 5), which is a clastic

352   sediment-starved carbonate platform setting, indicate that enhanced Hg influx from

353   terrestrial sources could be imported to oceans and overwhelmed the volcanic

354   signature from the Siberian Traps (Grasby et al., 2017). It is possible that most of Hg

355   coming from the terrestrial source might have also been derived from the STLIP and

356   this is indicated by the similar Hg/TOC baselines of the studied sections. The larger

357   spike at Meishan suggests a focusing of the volcanic Hg via the terrestrial ecosystems

358   to marine deposition above that of direct atmospheric inputs. Similarly, highest

359   Hg/TOC excursions were also noted in terrestrial and coastal sections by Percival et al.

360   (2015, 2017) who have reported Hg anomalies in several different sedimentary

361   records that span Pliensbachian-Toarcian transition and end-Triassic mass extinction.

362   For example, the Pliensbachian-Toarcian transition at Bornholm, Danish Basin, which

363   preserves a fluvial to marginal marine setting, shows greatest its Hg/TOC excursion

364   during the Toarcian Oceanic anoxic events. The end-Triassic record from a

365   fluvial-deltaic section of Astartekløft, Greenland, also shows its greatest Hg/TOC

366   excursion during the end-Triassic mass extinction interval. These suggest that the

367   different values in Hg/TOC at the EPME recorded in our studied sections are not due

368   to slightly different sampling resolution at the sites (e.g., lower resolution at

369   Daxiakou), rather they show that coastal/terrestrial sediments include additional

370   terrestrial Hg relative to deeper sections.

371   The Daxiakou and Shangsi sections both represent deeper water depositional

372   environments (~200–500 m) (Jiang et al., 2011; Zhao et al., 2013; Zhang and Gu,

373   2015; Xiao et al., 2017). At the EPME, the Daxiakou section is inferred to have been

374   at a greater water depth than the Shangsi section, based on its overall finer grain-size

375   of the sediment. The Δ^{199}Hg values of Daxiakou at the EPME have greater positive

376   values than those from Shangsi (Fig. 5), consistent with the Daxiakou section being

377   least affected by terrestrial Hg. The positive Δ^{199}Hg values at the EPME in the

378   Daxiakou and Shangsi sections are consistent with those observed in modern

379   sediments that receive insignificant terrestrial runoff (Thibodeau and Bergquist, 2017,

380   references therein), as well as those obtained from deeper water section across the

381   Cretaceous-Paleogene transition (Bajada del Jagüel section, Sial et al., 2016).

382   Conversely, no significant Hg-MIF (Δ^{199}Hg $\approx$ 0 ‰) signature with Hg enrichments

383   that was associated with an overloading of volcanic Hg from the Central Atlantic

384   Magmatic Province, was observed during end-Triassic mass extinction in a shallow

385   shelf sediments at Muller Canyon, Nevada (USA), indicating that the sediments

386   received volcanic Hg through both atmosphere Hg^{2+} deposition and terrestrial runoff,

387   and the Hg-MIF signatures were overwhelmed (Thibodeau et al., 2016; Thibodeau

388   and Bergquist, 2017).

389   In summary, sediments receive variable proportions of their Hg from direct

390   atmospheric and terrestrial inputs. It is likely that Hg, including Hg/TOC and Hg

391 isotopes in shallow water sections are more sensitive to terrestrial signals, such as the

392 portion of Hg entering from the atmosphere to land systems and ancient Hg

393 originating from eroding rocks. In contrast, deep water sections better record the

394 timing and strength of eruptions in the geological record because of their more precise

395 sensitivity to Hg atmospheric perturbations unmediated by the terrestrial realm

396 (Grasby et al., 2017; Thibodeau and Bergquist, 2017).

397

398 5.3 Causal links between biotic extinction and STLIP

399   The STLIP is recognized as the largest continental basalt province (Dobretsov et

400 al., 2008). The preserved area of the province is of the order of 2.5 million km^2 and a

401 working estimate for the total volume of eruptives and shallow-level intrusions is 3-4

402 million km^3 (Fedorenko et al., 2000). The coincidence of the STLIP with the EPME

403 (Wignall, 2001; Courtillot and Renne, 2003; Burgess and Bowing, 2015), suggests a

404 link between the two events. Release of volcanic CO_2 and thermogenic methane

405 through magma emplacement into the West Siberian Tunguska basin, which is

406 composed of a thick succession of evaporite, clastic, carbonate, and

407 hydrocarbon-bearing rocks, is thought to have triggered strong climatic warming and

408 ocean acidification (Svensen et al., 2009; Sun et al., 2012; Black et al., 2014;

409 Clarkson et al., 2015), as evidenced 3 to 4 ‰ negative shift in C-isotopic records

410 coincident with the EPME horizon (Fig. 5).

411   Siberian Traps magmatic activity is divided into three stages based on

412 high-precision U-Pb dates: early extrusion (252.24–251.907 Ma; ~C.

413 changxingenss–C. yini conodont zones), characterized by initial pyroclastic eruptions

414 followed by lava effusion, then medium-term sill intrusion (251.907–251.483 Ma; ~ C.

415 meishanensis–lower I. isarcica conodont zones), and terminal stage (lasting until at

416 least 251.354 Ma; above the lower I. isarcica conodont zone), marked by initial lava

417 extrusion after a ~420 ka hiatus and then sill intrusion (Burgess and Bowring, 2015;

418 Burgess et al., 2017). This implies that STLIP involved three or more original magma

419 pulses. Burgess et al. (2017) showed that the initial pulse of Siberian Traps sills

420 following the initial extrusive pyroclastics and lava, coincided with the onset of

421 EPME and an abrupt negative C isotope shift. Hg enrichment also occurs at that

422 horizon (this study; Sanei et al., 2012; Grasby et al., 2013; 2017). This suggests that a

423 large volume of Hg was released into the atmosphere at the time of initial sill

424 intrusion. Most of the sills are exposed at the periphery of exposures of lavas and

425 volcaniclastic rocks, and are up to 1200 m thick (Svensen et al., 2009; Burgess and

426 Bowring, 2015). Compared to the pyroclastic lava, the sills take up a much larger area

427 and volume (Vasiliev et al., 2000; Burgess and Bowring, 2015). Total sill volume in

428 the STLIP is difficult to constrain but has been conservatively estimated in excess of 2

429 $\times 10^6$ km^3 (Vasiliev et al., 2000), which maybe exceed 50 % of the STLIP's total

430 volume. Such massive sills provided extensive horizontal and vertical magmatic

431 channels and diatremes, by which volatiles are delivered to the atmosphere (Svensen

432 et al., 2009; Burgess et al., 2017). As a heat sensitive element, the major proportion of

433 Hg in sedimentary rocks is released if the temperature exceeds 340 $^{\circ}$C (Sial et al.,

434 2013). Therefore, during the early intrusion stage, massive gas Hg^0 would be

435   produced by interaction between the magma and country rocks and easily released to

436   the atmosphere through magmatic vents (Burgess et al., 2017). The Hg content of

437   mantle material is 0.01 µg/g (McDonough, 2003). Using a density of basic rock of

438   2.8×10^3 kg/m^3, total Hg released from 2×10^6 km^3 sills would be 5.6×10^9 Mg. A

439   similar estimated value of 3.8×10^9 Mg was given by Sanei et al. (2012). In addition,

440   heating of sediments over the large area encompassed by the sill complex could

441   provide additional Hg release, the estimated quantity of which is about 1.75×10^5 Mg

442   (Sanei et al., 2012). If most of the 2×10^6 km^3 sills intruded during 251.907–251.483

443   Ma, then 13000 Mg yr^{-1} volcanic Hg would be released to the atmosphere during that

444   time, which is ~5.6 times current anthropogenic emissions of ~2320 Mg yr^{-1} and is

445   ~144.4 times modern volcanic emissions of ~90 Mg yr^{-1} (Pirrone et al., 2010; Sial et

446   al., 2013). The general elevation of Hg/TOC values in the C. meishanensis–lower I.

447   isarcica conodont zones, marked by green on figure 5, corresponds with the high rate

448   of Hg emission during the Siberian sill emplacement. Furthermore, the highest values

449   at the EPME correspond to the strongest release. Depending on the high rate of

450   emission, the enhanced Hg release at the EPME horizon may have temporarily

451   exceeded the capacity of organic matter to fix Hg resulting in its buildup in ocean

452   water to toxic levels (Sanei et al., 2015).

453   Other than a direct link by poisoning, most extinction scenarios invoke a

454   volcanism-extinction nexus caused by the subsequent effects of CO_2 release and rapid

455   global warming (Sun et al., 2012), which include ocean anoxia, acidification, and the

456   direct consequences of warming. Such effects are longer term than direct Hg

457 poisoning which, if significant, is likely to have occurred on a timescale of decades to

458 centuries because of the short residence time of this element in the ocean-atmosphere

459 system. Carbon dioxide-driven global warming is a longer term effect (centuries,

460 millennia) because of the longer residence time in the Earth surface system (Wignall,

461 2001). Nonetheless, our data show a tight coincidence between the onset of extinction

462 in South China and Hg enrichment. Any lead in time between the onset of STLIP

463 volcanism and the environmental consequences was below the temporal resolution of

464 our study. Phrased another way, the devastation caused by the onset of Siberian Trap

465 sill emplacement was geologically instantaneous.

466 **6. Conclusions**

467   Three sections across the end-Permian mass extinction at Meishan, Daxiakou,

468 and Shangsi in South China all record high Hg concentrations and a short-lived

469 positive excursion in Hg/TOC values. Hg isotopes with positive values (Δ^{199}Hg) and

470 limited variability in the Daxiakou and Shangsi sections indicate a predominant

471 atmospheric-derived Hg signature from STLIP, whereas in the Meishan section,

472 δ^{202}Hg and Δ^{199}Hg both display negative shifts, indicating a significant proportion of

473 terrestrial sources (Grasby et al., 2017). Our data indicate that Hg, including Hg/TOC

474 and Hg isotopes, show different geochemical behavior at different water depths. For

475 Meishan, a clastic sediment-starved carbonate platform setting, enhanced Hg influx

476 from terrestrial sources could be imported to the marine setting and overwhelmed the

477 volcanic signature from Siberian Traps. At the deeper water marine sections, at

478   Daxiakou and Shangsi, a lower terrestrial signature was recorded. Although more

479   studies are undoubtedly needed on the geochemical behavior of Hg in different

480   sedimentary facies, our finding suggests that deep water marine facies can more

481   directly record the atmospheric-derived Hg signature from volcanism than near shore

482   shallow marine environments where signals are mediated to a greater extent by

483   terrestrial ecosystems via continental run off. Furthermore, our study demonstrates

484   that the effects of the STLIP extended to the Chinese sections, and clarifies the

485   relationship between Siberian eruptions and the EPME in South China.

486

498

499

500

References

502   Bergquist, B.A., Blum, J.D., 2007. Mass-dependent and -independent fractionation of

503   Hg isotopes by photoreduction in aquatic systems. Science 318, 417–420.

504   Black, B.A., Lamarque, A.F., Shields, C.A., Elkins-Tanton, L.T., Kiehl, J.T., 2014.

505   Acid rain and ozone depletion from pulsed Siberian Traps magmatism. Geology

506   42, 67–70.

507   Blum, J.D., Sherman, L.S., Johnson, M.W., 2014. Mercury isotopes in earth and

508   environmental sciences. Annu. Rev. Earth Planet. Sci. Lett. 42, 249–269.

509   Burgess, S.D., Bowring, S.A., Shen, S.Z., 2014. High-precision timeline for Earth's

510   most severe extinction. Proc. Natl. Acad. Sci. U. S. A. 111, 3316–3321.

511   Burgess, S.D., and Bowring, S.A., 2015. High-precision geochronology confirms

512   voluminous magmatism before, during, and after Earth's most severe extinction.

513   Sci. Adv. 1: 1500470e.

514   Burgess, S.D., Muirhead, J.D., Bowring, S.A., 2017. Initial pulse of Siberian Traps

515   sills as the trigger of the end-Permian mass extinction. Nat. Commun. 8, 164.

516   Chen, Z.Q., Yang, H., Luo, M., Benton, M.J., Kaiho, K., Zhao, L.S., Huang, Y.G.,

517   Zhang, K.X., Fang, Y.H., Jiang, H.S., Qiu, H., Li, Y., Tu, C.Y., Shi, L., Zhang, L.,

518   Feng, X.Q., Chen, L., 2015. Complete biotic and sedimentary records of the

519   Permian–Triassic transition from Meishan section, South China: ecologically

520   assessing mass extinction and its aftermath. Earth-Sci. Rev. 149, 67–107.

521   Clarkson, M.O., Kasemann, S.A., Wood, R.A., Lenton, T.M., Daines, S.J., Richoz, S.,

522   Ohnemueller, F., Meixner, A., Poulton, S.W., Tipper, E.T., 2015. Ocean

523   acidification and the Permo-Triassic mass extinction. Science34 8, 229–232.

524 Courtillot, V.E., Renne, P.R., 2003. On the ages of flood basalt events. C. R.

525   Geoscience 335, 113–140.

526 Dobretsov, N.L., Kirdyashkin, A.A., Kirdyashkin, A.G., Vernikovsky, V.A., Gladkov,

527   I.N., 2008. Modelling of thermochemical plumes and implications for the origin

528   of the Siberian traps. Lithos 100, 66–92.

529 Feng, Z., Yang, Y., Jin, Z., He, Y., Wu, S., Xin, W., Bao, Z., Tan, J., 1996.

530   Lithofacies paleogeography of the Permian of South China. Acta

531   Sedimentologica Sinica 14, 1–11.

532 Fedorenko, V., Czamanske, G., Zen'ko, T., Budahn, J., Siems, D., 2000. Field and

533   geochemical studies of the melilite-bearing Arydzhangsky Suite, and an overall

534   perspective on the Siberian alkaline-ultramafic flood volcanic rocks. Int. Geol.

535   Rev. 42, 769–804.

536 Grasby, S.E., Sanei, H., Beauchamp, B., Chen, Z.H., 2013. Mercury deposition

537   through the Permo–Triassic biotic crisis. Chem. Geol. 351, 209–216.

538 Grasby, S.E., Shen, W.J., Yin, R.S., Gleason, G.D., Blum, J.D., Lepak, R.F., Hurley,

539   J.P., Beauchamp, B., 2017. Isotopic signatures of mercury contamination in latest

540   Permian Oceans. Geology 45, 55–58.

541 Gehrke, G.E., Blum, J.D., Meyers, P.A., 2009. The geochemical behaviour and

542   isotopic composition of Hg in a mid-Pleistocene western Mediterranean sapropel.

543   Geochim. Cosmochim. Acta 73, 1651–1665.

544   Jiang, H.S., Lai, X.L., Yan, C.B., Aldridge, R.J., Wignall, P., Sun, Y.D., 2011. Revised

545   conodont zonation and conodont evolution across the Permian–Triassic boundary

546   at the Shangsi section, Guangyuan, Sichuan, South China. Global and Planetary

547   Change 77, 103–115.

548   Li, Z.S., Zhan, L.P., Zhu, X.F., Zhang, J.H., Jin, R.G., Liu, G.F., Sheng, H.B., Shen,

549   G.M., Dai, J.Y., Huang, H.Q., Xie, L.C., Yan, Z., 1986. Mass extinction and

550   geological events between Palaeozoic and Mesozoic era. Acta geological sinica

551   60, 1–15 (in Chinese with English abstract).

552   Li, M.S., Ogg, J., Zhang, Z., Huang, C.J., Hinnov, L., Chen, Z.Q., Zou, Z.Y., 2016.

553   Astronomical tuning of the end-Permian extinction and the Early Triassic Epoch

554   of South China and Germany. Earth Planet. Sci. Lett. 441, 10–25.

555   Liu, S.A., Wu, H.C., Shen, S.Z., Jiang, G.Q., Zhang, S.H., Lv, Y.W., Zhang, H., Li,

556   S.G., 2017. Zinc isotope evidence for intensive magmatism immediately before

557   the end-Permian mass extinction. Geology 45, 343–346.

558   McDonough, W. F., 2003. Compositional model for the Earth's core. Treatise on

559   geochemistry 2, 568.

560   Payne, J.L., Turchyn, A.V., Paytan, A., DePaolo, D.J., Lehrmann, D.J., Yu, M.Y., Wei,

561   2010. J.Y., Calcium isotope constraints on the end-Permian mass extinctions.

562   PNAS 107, 8543–8548.

563   Percival, L.M.E., Witt, M.L.I., Mather, T.A., Hermoso, M., Jenkyns, H.C., Hesselbo,

564   S.P., Al-Suwaidi, A.H., Storm, M.S., Xu, W., Ruhl, M., 2015. Globally enhanced

565   mercury deposition during the end-Pliensbachian extinction and Toarcian OAE:

566   A link to the Karoo–Ferrar Large Igneous Province. Earth Planet. Sci. Lett. 428,

567   267–280.

568 Percival, L.M.E., Ruhl, M., Hesselbo, S.P., Jenkyns, H.C., Mather, T.A., Whiteside,

569   J.H., 2017. Mercury evidence for pulsed volcanism during the end-Triassic mass

570   extinction. Proc. Natl. Acad. Sci. U. S. A. 114, 7929–7934.

571 Pirrone, N., Cinnirella, S., Feng, X., Finkelman, R.B., Friedli, H.R., Leaner, J., Mason,

572   R., Mukherjee, A.B., Stracher, G.B., Streets, D.G., Telmer, K., 2010. Global

573   mercury emissions to the atmosphere from anthropogenic and natural sources.

574   Atmos. Chem. Phys. Discuss. 10, 4719–4752.

575 Pyle, D.M., Mather, T.A., 2003. The importance of volcanic emissions for the global

576   atmospheric mercury cycle. Atmos. Environ. 37, 5115–5124

577 Gong, Q., Wang, X.D., Zhao, L.S., Grasby, S.E., Chen, Z.Q., Zhang, L., Li, Y., Cao,

578   L., Li, Z.H., 2017. Mercury spikes suggest volcanic driver of the

579   Ordovician-Silurian mass extinction. Sci.Rep. 7, 5304.

580 Reichow, M.K., Pringle, M.S., Al'Mukhamedov, A.I., Allen, M.B., Andreichev, V.L.,

581   Buslov, M.M., Davies, C.E., Fedoseev, G.S., Fitton, J.G., Inger, S., Medvedev,

582   A.Y., Mitchell, C., Puchkov, V.N., Safonova, I.Y., Scott, I.A., Saunders, A.D.,

583   2009. The timing and extent of the eruption of the Siberian Traps large igneous

584   province: Implications for the end-Permian environmental crisis. Earth Planet.

585   Sci. Lett. 277, 9–20.

586 Riccardi, A., L Kump, R., Arthur, M.A., D'Hondt, S., 2007. Carbon isotopic evidence

587   for chemocline upward excursions during the end-Permian event. Palaeogeogr.

588   Palaeoclimatol. Palaeoecol. 248, 73–81.

589   Ruiz, W.L.G., and Tomiyasu, T., 2015. Distribution of mercury in sediments from

590   Kagoshima Bay, Japan, and its relationship with physical and chemical factors.

591   Environ. Earth Sci. 74, 1175–1188.

592   Sanei, H., Grasby, S.E., Beauchamp, B., 2012. Latest Permian mercury anomalies.

593   Geology 40, 63–66.

594   Sanei, H., Grasby, S.E., Beauchamp, B., 2015. Contaminants in marine sedimentary

595   deposits from coal fly ash during the latest Permian extinction. Develop.

596   Paleoenviron. Res. 18, 89–99.

597   Saunders, A.D., 2016. Two LIPs and two Earth-system crises: the impact of the North

598   Atlantic Igneous Province and the Siberian Traps on the Earth-surface carbon

599   cycle. Geol. Mag. 153, 201–222.

600   Sial, A.N., Lacerda, L.D., Ferreira, V.P., Frei, R., Marquillas, R.A., Barbosa, J.A.,

601   Gaucher, C., Windmöller, C.C., Pereira, N.S., 2013. Mercury as a proxy for

602   volcanic activity during extreme environmental turnover: The

603   Cretaceous–Paleogene transition. Palaeogeogr. Palaeoclimatol. Palaeoecol. 387,

604   153–164.

605   Sial, A.N., Chen, J.B., Lacerda, L.D., Frei, R., Tewari, V.C., Pandit, M.K., Gaucher,

606   C., Ferreira, V.P., Cirilli, S., Peralta, S., Korte, C., Barbosa, J.A., Pereira, N.S.,

607   2016. Mercury enrichment and Hg isotopes in CretaceousePaleogene boundary

608   successions: Links to volcanism and palaeoenvironmental impacts. Cretaceous

609   Res. 66, 60–81.

610   Shen, S.Z., Crowley, J.L., Wang, Y., Bowring, S.A., Erwin, D.H., Sadler, P.M., Cao,

611   C.Q., Rothman, D.H., Henderson, C.M., Ramezani, J., Zhang, H., Shen, Y.N.,

612   Wang, X.D., Wang, W., Wu, L., Li, W.Z., Tang, Y.G., Liu, X.L., Liu, L.J., Zeng,

613   Y., Jin, Y.G., 2011, Calibrating the end-Permian mass extinction. Science 334,

614   1367–1372.

615   Shen, J., Feng, Q.L., Algeo, T.J., Li, C., Planavsky, N.J., Zhou, L., Zhang, M.L., 2016.

616   Two pulses of oceanic environmental disturbance during the Permian–Triassic

617   boundary crisis. Earth Planet. Sci. Lett. 443, 139–152.

618   Song, H.Y., Song, H.J., Algeo, T.J., Tong, J.N., Romaniello, S.R., Zhu, Y.Y., Chu,

619   D.L., Gong, Y.M., Anbar, A.D., 2017. Uranium and carbon isotopes document

620   global-ocean redoxproductivity relationships linked to cooling during the

621   Frasnian- Famennian mass extinction. Geology 45, 887–890.

622   Sun, Y.D., Joachimski, M.M., Wignall, P.B., Yan, C.B., Chen, Y.L., Jiang, H.S.,

623   Wang, L.N., Lai, X.L., 2012. Lethally Hot Temperatures during the Early

624   Triassic Greenhouse. Science 338, 366-370.

625   Svensen, H., Planke, S., Polozov, A.G., Schmidbauer, N., Corfu, F., Podladchikov,

626   H.H., Jamtveit, B., 2009. Siberian gas venting and the end-Permian

627   environmental crisis. Earth Planet. Sci. Lett. 277, 490–500.

628   Thibodeau, A.M., Ritterbush, K., Yager, J.A., West, A.J.,Ibarra, Y., Bottjer, D.J.,

629   Berelson, W.M., Bergquist, B.A., Corsetti, F.A., 2016. Mercury anomalies and

630   the timing of biotic recovery following the end-Triassic mass extinction. Nat.

631   Commun. 7, 11147.

632   Thibodeau, A.M., Bergquist, B.A., 2017. Do mercury isotopes record the signature of

633   massive volcanism in marine sedimentary records. Geology 45, 96–96.

634   Vasiliev, Y.R., Zolotukhin, V.V., Feoktistov, G.D., Prusskaya, S. N., 2000.

635   Evaluation of the volumes and genesis of the Permo–Triassic trap magmatism on

636   the Siberian platform. Russ. Geol. Geophys 41, 1696–1705.

637   Wignall, P.B., Hallam, A., Lai, X.L., Yang, F.Q., 1995. Paleoenvironmental changes

638   across the Permian/Triassic boundary at Shangsi (N. Sichuan, China). Hist.

639   Biol. 10, 175–189.

640   Wignall, P.B., 2001. Large provinces and mass extinctions. Earth Sci. Rev. 53, 1-33.

641   Xiang, L., Schoepfer, S.D., Zhang, H., Yuan, D.X., Cao, C.Q., Zheng, Q.F.,

642   Henderson, C.M., Shen, SZ., 2016. Oceanic redox evolution across the

643   end-Permian mass extinction at Shangsi, South China. Palaeogeogr.

644   Palaeoclimatol. Palaeoecol. 448, 59–71.

645   Xiao, Y.F., Suzukib, N., He, W.H., 2017. Water depths of the latest Permian

646   (Changhsingian) radiolarians estimated from correspondence analysis. Earth-Sci.

647   Rev. 173, 141–158.

648   Yin, H.F., Zhang, K.X., Tong, J.N., Yang, Z.Y., Wu, S.B., 2001. The global stratotype

649   section and point (GSSP) of the Permian-Triassic boundary. China basic science

650   24, 102–114.

651   Yin, R., Feng, X., Hurley, J.P., Krabbenhoft, D.P., Lepak, R.F., Hu, R., Zhang, Q., Li,

652   Z., Bi, X., 2016. Mercury isotopes as proxies to identify sources and

653   environmental impacts of mercury in sphalerites. Sci. Rep. 6, 18686.

654   Zambardi, T., Sonke, J.E., Toutain, J.P., Sortino, F., Shinohara, H., 2009. Mercury

655   emissions and stable isotopic compositions at Vulcano Island (Italy). Earth

656   Planet. Sci. Lett. 277, 236–243.

657   Zhao, L.S., Chen, Y.L., Chen, Z.Q., Cao, L., 2013. Uppermost Permian to Lower

658   Triassic conodont zonation from three gorges area, South China. Palaios 28,

659   523–540.

660   Zhang, M.H., Gu, S.Z., 2015. Latest Permian deep-water foraminifers from Daxiakou,

661   Hubei, South China. J. Paleontol. 89, 448–464.

662

663

664

665

666   **Figure captions:**

667

668   **Fig. 1 Global (A) and South China (SC) (B) paleogeographic configurations over**

669   **the Permian-Triassic transition showing the locations of the Meishan (MS),**

670   **Daxiakou (DXK) and Shangsi (SS) sections, and the Siberia Traps large igneous**

671   **province (STLIP).** Global paleographic map is available online

672   http://jan.ucc.nau.edu/~rcb7/, and map B follows Feng et al. (1996).

673

674   **Fig. 2 TOC, Hg, Hg/TOC and Hg isotopic compositions over the**

675   **Permian–Triassic transition at the Meishan section, South China**. Hg, Hg/TOC

676   ratios and Hg isotopes through bed 24 to bed 29 are from Grasby et al. (2017), and

677   shown by red circles. Sedimentation rates (SR) are calculated by Li et al. (2016)'s age

678   model. Conodont zones follow Chen et al. (2015).
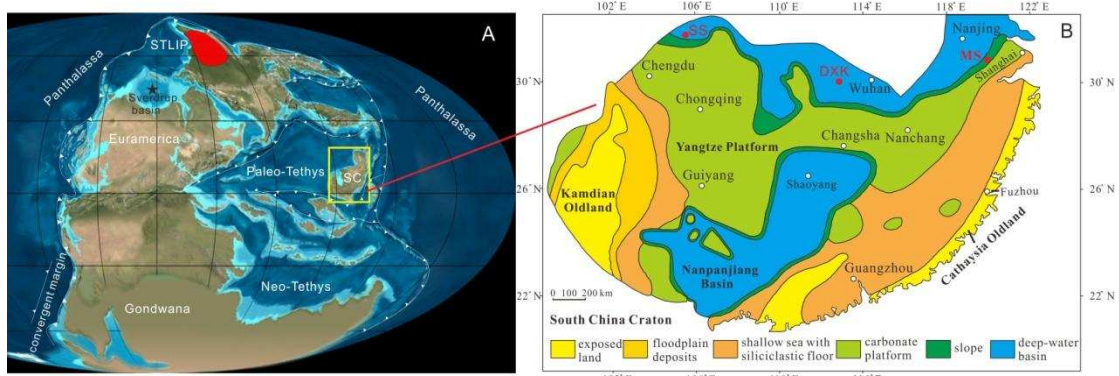
679

680

681   **Fig. 3 TOC, Hg, Hg/TOC and Hg isotopic compositions over the**

682   **Permian–Triassic transition at the Daxiakou section, South China**. Sedimentation

683   rates (SR) are calculated by Li et al. (2016)'s age model. Conodont zones follow Zhao

684   et al. (2013).

685

686   **Fig. 4 TOC, Hg, Hg/TOC and Hg isotopic compositions over the**

687   **Permian–Triassic transition at the Shangsi section, South China.** Conodont zones

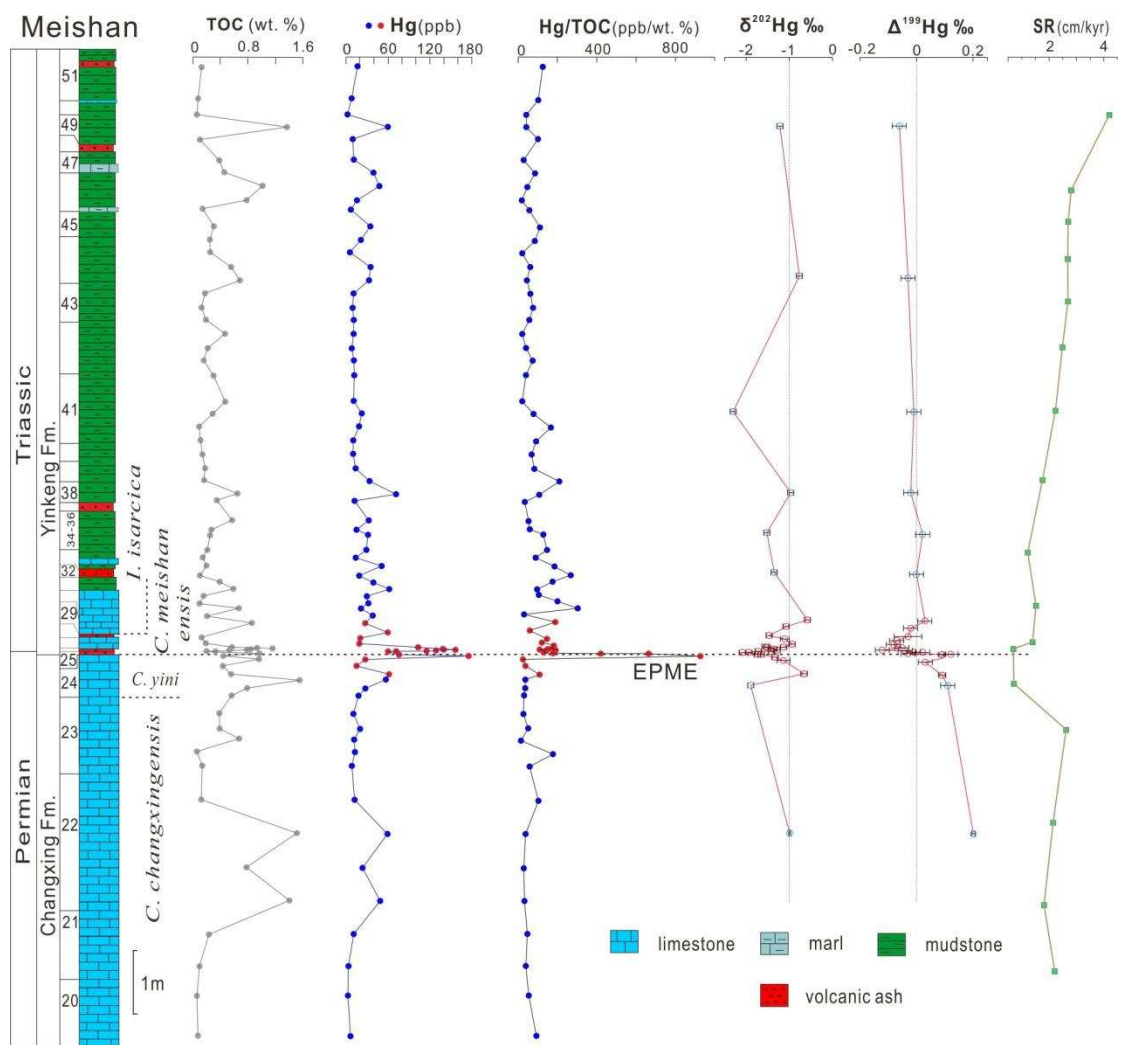688   follow Jiang et al. (2011).

689

690   **Fig. 5 Integrated excursions of Hg/TOC ratios, Hg isotopes, δ^{13}C values (Burgess**

691   **et al., 2014), species richness variations (Song et al., 2013) and STLIP stages**

692   **(Burgess et al., 2017) over the Permian–Triassic transition.** Ages are from

693   Meishan section reported by Burgess et al. (2014)**.** C = Clarkina, H = Hindeodus, I =
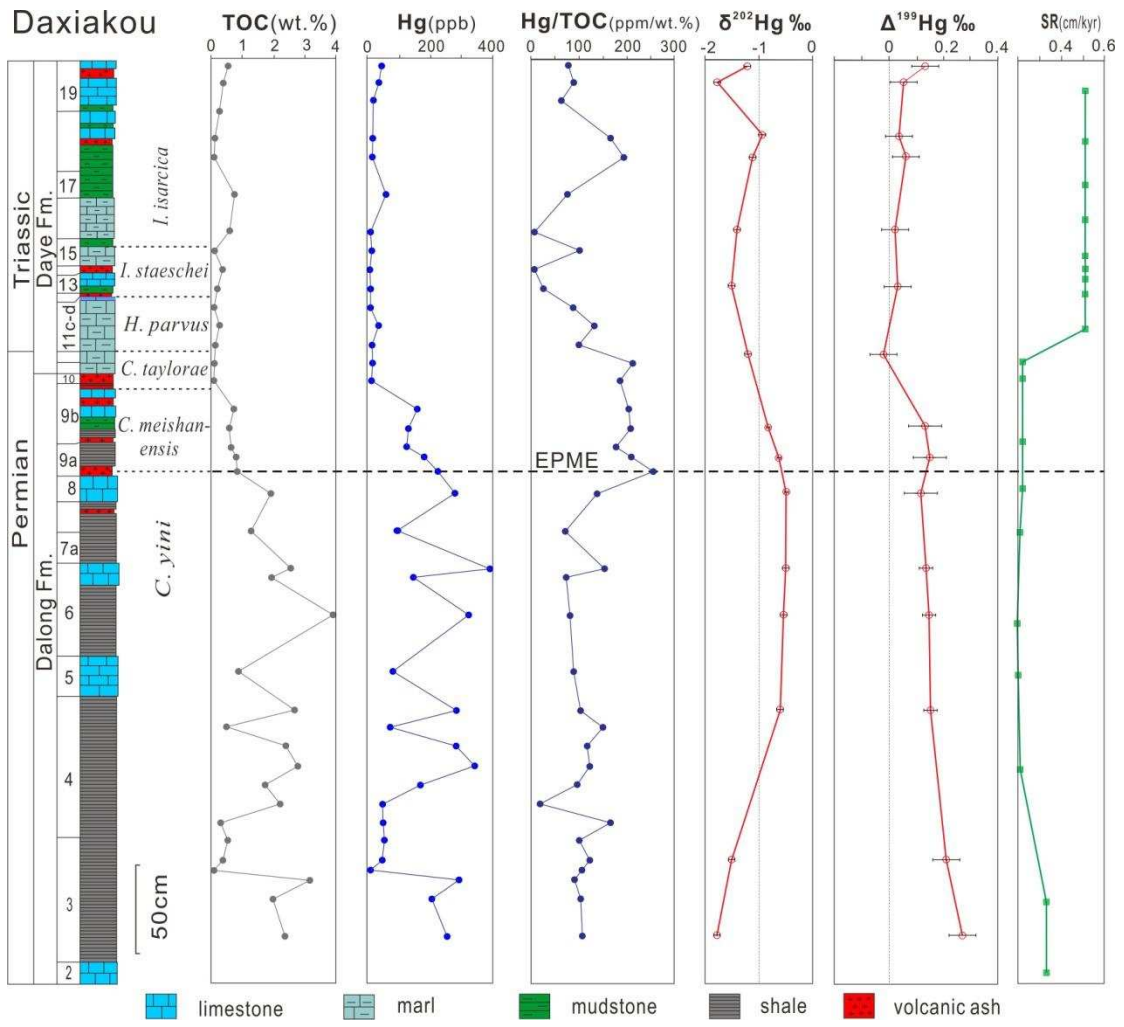
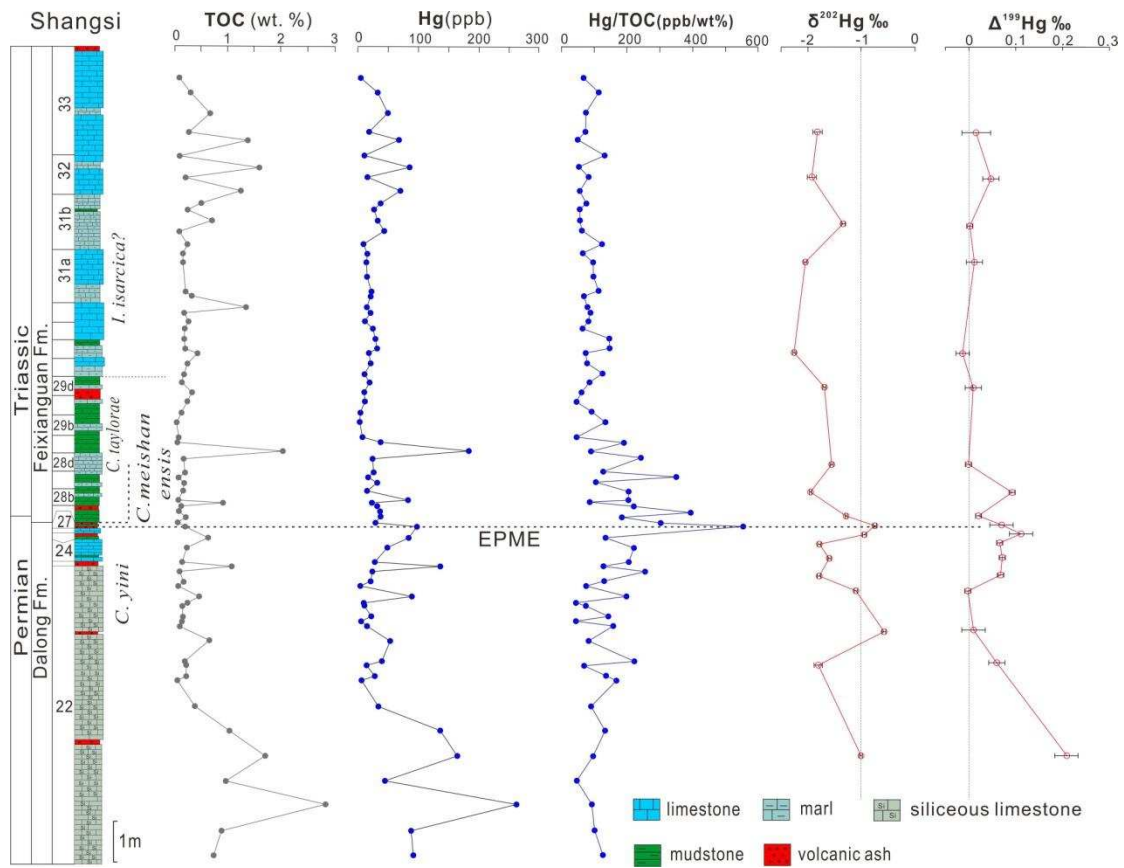694   Isarcicella

695

Fig. 1

697

698
699

Fig. 2

701

702

703

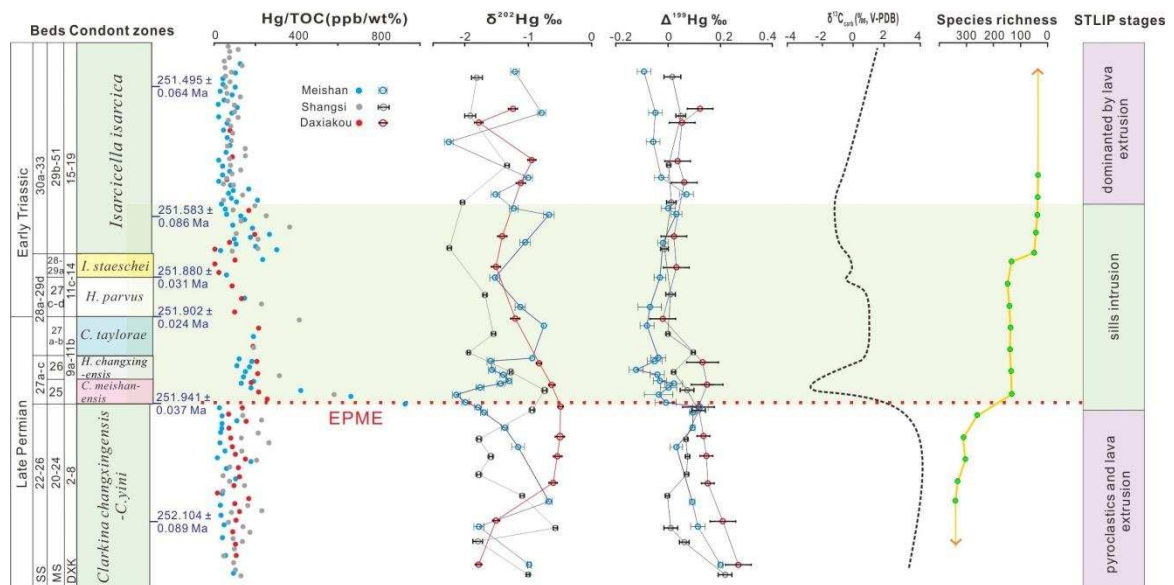704 Fig. 3

705

706

Fig. 4

707

708

709

Fig. 5

710

711

35